

insulator scenario at low energy.

I. THEORETICAL APPROACH

A charge self-consistent combination of density functional theory and dynamical mean-field theory (DMFT) is employed¹⁵. The mixed-basis pseudopotential method^{16,17}, based on norm-conserving pseudopotentials with a combined basis of localized functions and plane waves is used for the DFT part with the generalized-gradient approximation in form of the PBE functional¹⁸. Within the mixed basis, localized functions for Cr(3*d*), Pd(4*d*) and Ag(4*d*) states as well as for O(2*s*) and O(2*p*) are utilized to reduce the plane-wave energy cutoff. The latter is chosen $E_{\text{cut}} = 20$ Ryd for the bulk structures and $E_{\text{cut}} = 16$ Ryd for the heterostructures. A \mathbf{k} -point mesh of $13 \times 13 \times 13$ partition is utilized for the bulk structures and of $11 \times 11 \times 3$ partition for the heterostructures.

The correlated subspace for the DMFT part consists of the effective Cr(3*d*) Wannier-like functions as obtained from the projected-local-orbital formalism^{19,20}, using as projection functions the linear combinations of atomic 3*d* orbitals, diagonalizing the Cr(3*d*) orbital-density matrix. A five-orbital Slater-Kanamori Hubbard Hamilto-

nian governs the interacting electrons, parametrized by a Hubbard U and a Hund's exchange J_{H} . The coupled single-site DMFT impurity problems in the given structures are solved by the continuous-time quantum Monte Carlo scheme^{21,22} as implemented in the TRIQS package^{23,24}. A double-counting correction of fully-localized-limit type²⁵ is applied. No Hubbard interactions are applied to Pd(4*d*) and Ag(4*d*). Such interactions are already expected much smaller than on Cr(3*d*) and then furthermore their effect onto nominal $d^9(d^{10})$ of Pd(Ag) should be weak in the metallic-layer architecture. Thus restricting the explicit DMFT-impurity treatment to the Cr sites is sound to study key correlation effects.

To obtain the spectral information, analytical continuation from Matsubara space via the maximum-entropy method as well as the Padé method is performed. In the former case, the \mathbf{k} -integrated Bloch Green's functions are continued, whereas in the latter case the local Cr self-energies are continued. If not otherwise stated, the maximum-entropy scheme is chosen to reveal \mathbf{k} -integrated spectral functions and the Padé scheme is chosen to obtain \mathbf{k} -resolved spectral functions. Note moreover that the \mathbf{k} -resolved spectral functions are computed on a dense mesh along high-symmetry lines and in the $k_z = 0$ plane of reciprocal space. For this purpose, the converged real-frequency local self-energies from the Padé scheme, and the self-consistent projected-local-orbitals recomputed on the dense mesh, are utilized to obtain well-resolved Green's functions in \mathbf{k} -space.

The DFT+DMFT calculations are conducted by setting the system temperature to room temperature $T = 290$ K, if not otherwise stated. Paramagnetism is as-

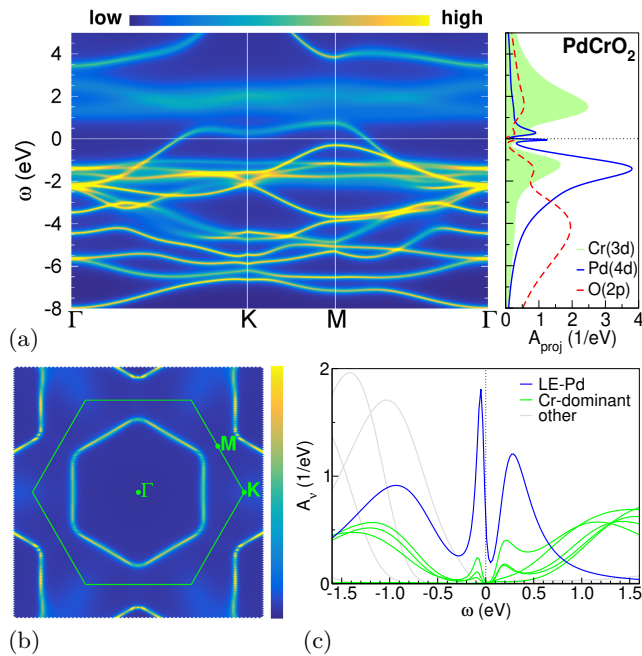


FIG. 2. (color online) Spectral data of PdCrO₂. (a) Spectral function $A(\mathbf{k}, \omega)$ along high-symmetry lines in the $k_z = 0$ plane of reciprocal space (left) and \mathbf{k} -integrated site- and orbital-projected spectral function (right). (b) Fermi surface for $k_z = 0$ within the first Brillouin zone (green hexagon) and (c) \mathbf{k} -integrated Bloch contribution $A_\nu(\omega)$ (i.e. each individual curve marks a different Bloch index ν) with characterization of site dominance. Note that the following figures use the same normalized color scale for the \mathbf{k} -resolved spectral function as (a) and (b).

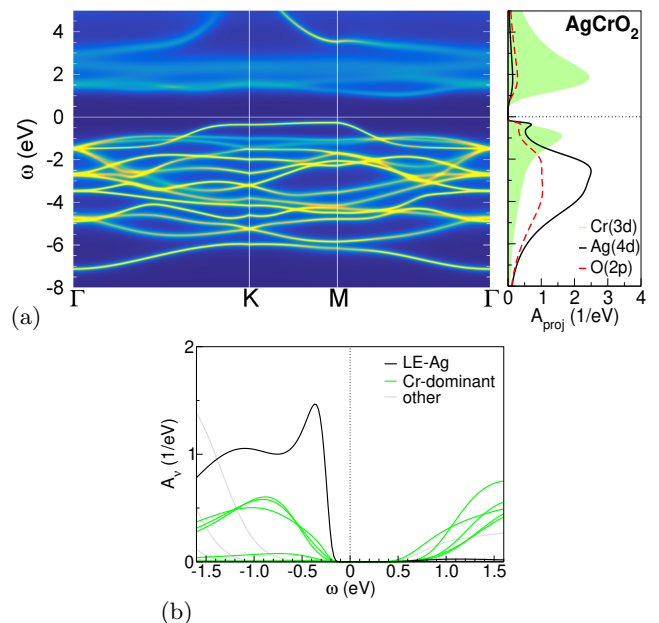


FIG. 3. (color online) Spectral data of AgCrO₂. (a) Spectral function $A(\mathbf{k}, \omega)$ as in Fig 2a. (b) \mathbf{k} -integrated Bloch contribution $A_\nu(\omega)$ as in Fig 2c.

sumed in all the computations. Furthermore in the following, if not otherwise stated, all shown spectral data is obtained from charge self-consistent DFT+DMFT calculations.

II. RESULTS

A. PdCrO₂ and AgCrO₂

To set the stage, we first briefly focus on the electronic structure of the natural bulk systems PdCrO₂ and AgCrO₂. Experimental lattice parameters^{1,5} $a = 2.930 \text{ \AA}$ and $c = 18.087 \text{ \AA}$ for PdCrO₂ as well as $a = 2.985 \text{ \AA}$

and $c = 18.510 \text{ \AA}$ for AgCrO₂ are used. The internal degree of freedom z , governing the oxygen distance to the A^+ plane is obtained from DFT structural optimization, reading $z = 0.1101 (0.1095)$ for PdCrO₂(AgCrO₂). Figures 2, 3 present a summary of the spectral characteristics. For PdCrO₂, local Coulomb interactions on the chromium site of $U = 3 \text{ eV}$ and $J_H = 0.7 \text{ eV}$ prove adequate as discussed in Ref. 10. The system is metallic with a single conducting Pd-dominated (cPd) quasiparticle dispersion at the Fermi level ε_F and Mott-insulating CrO₂ layers (see Fig. 2a). The cPd dispersion is dominantly formed by a linear combination of in-plane $d_{x^2-y^2}$ and d_{xy} , as well as by some d_{z^2} contribution (see Ref. 10 for more details). Note that the \mathbf{k} -integrated projected spectral function $A_{\text{proj}}(\omega)$ still displays sizable Cr-weight at low energy, associated with the cPd band. Thus intricate hybridization between the conducting and the Mott-insulating layers is at play¹⁰. The single-sheet Fermi surface, shown in Fig. 2b, is of hole kind and of hexagonal shape, in line with photoemission^{9,26}. It is furthermore instructive to visualize the spectral functions $A_\nu(\omega)$ with Bloch index ν . The function $A_\nu(\omega)$ amounts to \mathbf{k} -integrated spectral weight of the correlated system per Bloch state, i.e. it provides the spectral information of the correlated material as represented in Bloch Hilbert space. The total spectral function then reads $A_{\text{tot}}(\omega) = \sum_\nu A_\nu(\omega)$. Figure 3c shows that dominantly, there is a single- ν low-energy Pd-dominated (LE-Pd) contribution at the Fermi level. Be still aware that the complete cPd spectral weight consists of the low-energy ν -sum of all Bloch spectra.

In the case of AgCrO₂, the quasi closed-shell character of Ag reduces the screening within the CrO₂ subsystem and we therefore increased the Hubbard interaction on Cr to $U = 4 \text{ eV}$. Figure 3a,b exhibits that the CrO₂ layers remain Mott insulating, but the previously conducting band becomes completely filled and thus the system as a whole insulating. Hence AgCrO₂ is a combined band-Mott insulator. The obtained charge gap of $\sim 1.8 \text{ eV}$ is in good agreement with experiment. Note that the valence-band maximum is of mixed Ag, O character, while the conduction-band minimum of dominant Cr upper-Hubbard band character. Notably, whereas the Pd(4d) states in PdCrO₂ align with the Cr lower Hubbard band, the Ag(4d) states align with O(2p).

Let us comment on another important aspect, namely the evolution from the DFT electronic structure towards the fully-interacting one. When turning on interactions, the electronic spectrum in CrO₂-based delafossites does not evolve from a non-interacting(-like) band structure to a Mott-insulating spectrum, as observed for common Mott insulators²⁷. For instance in PdCrO₂, the metallic band structure evolves to another metallic spectrum, both spectra with weakly-correlated-looking dispersions at low energy. This interaction evolution takes place in a highly nontrivial way, as depicted in Fig. 4. In the DFT ($U = J_H = 0$) case, the three Cr-based t_{2g} bands cross the Fermi level and the later cPd band is still

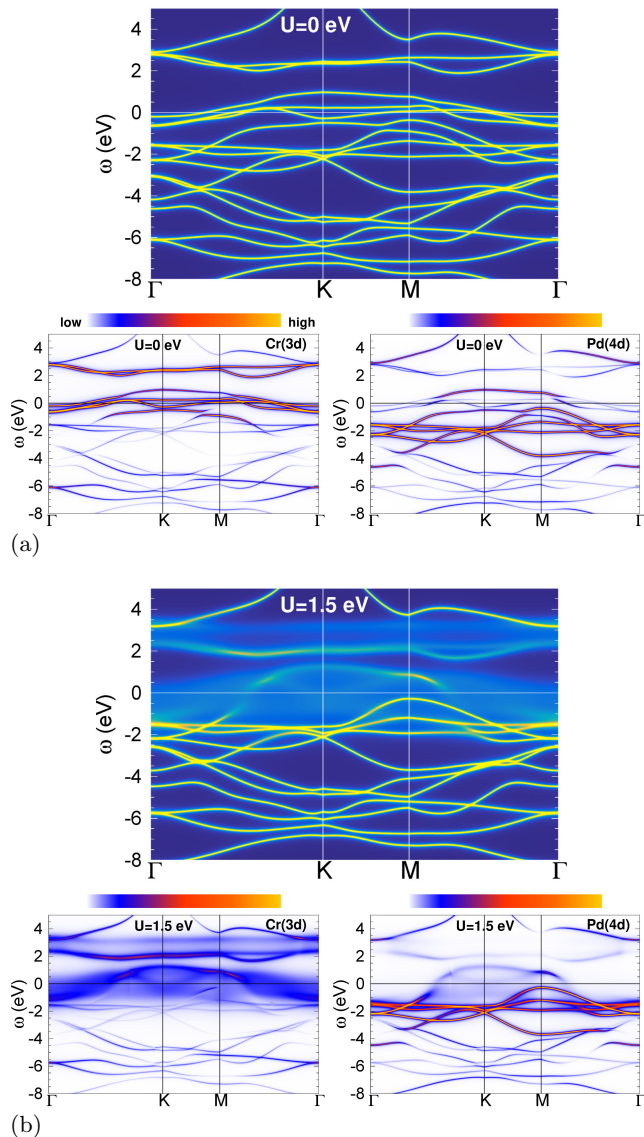


FIG. 4. (color online) \mathbf{k} -resolved spectral function (top) as well as Cr(3d)- and Pd(4d)-resolved spectral-function weight (bottom) of PdCrO₂ for (a) $U = J_H = 0$ (i.e. DFT band structure) and for (b) $U = 1.5 \text{ eV}$, $J_H = 0.35 \text{ eV}$.

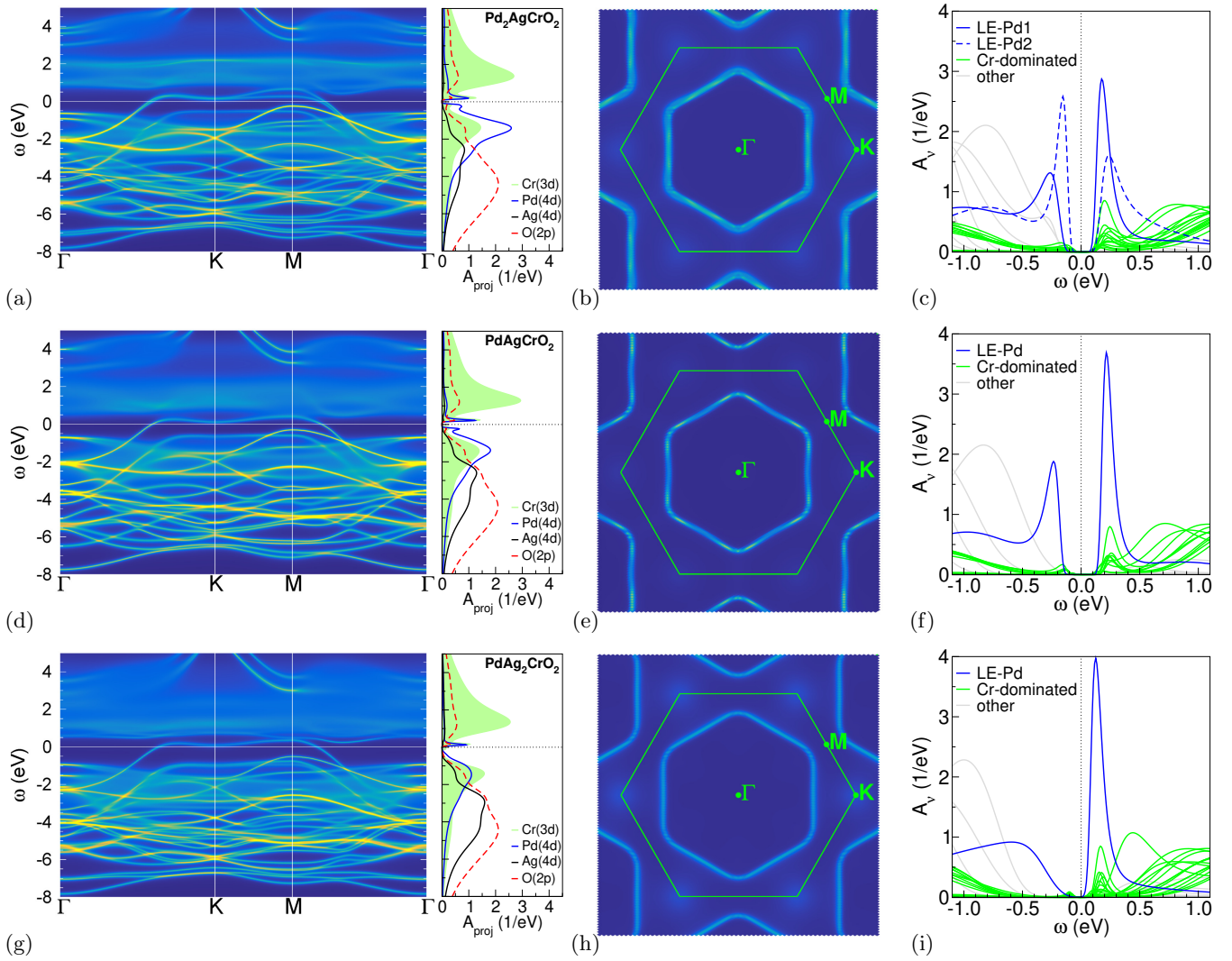


FIG. 5. (color online) Spectral data of the designed heterostructures: (a-c) $\text{Pd}_2\text{AgCrO}_2$, (d-f) PdAgCrO_2 and (g-i) $\text{PdAg}_2\text{CrO}_2$ at $T = 290$ K. (a,d,g) Spectral function $A(\mathbf{k}, \omega)$ along high-symmetry lines in the $k_z = 0$ plane of reciprocal space (left) and \mathbf{k} -integrated site- and orbital-projected spectral function (right). (b,e,h) Fermi surface for $k_z = 0$ within the first Brillouin zone (green hexagon). (c,f,i) \mathbf{k} -integrated Bloch contribution $A_\nu(\omega)$ with characterization of dominance.

completely filled well below ε_F , as visualized from the orbital-resolved spectral-function weights at the bottom of Fig. 4a. For $U = 1.5$ eV, $J_H = 0.35$ eV, (i.e. half the interaction strength of the true system) the CrO_2 layers are not yet Mott insulating, and the former Cr-based t_{2g} bands are now strongly incoherent even close to the Fermi level. Furthermore, the later cPd band also becomes very incoherent when entering the low-energy regime (cf. Fig. 4b). These incoherent features may be observed from the spreading of the spectral weight (i.e. “blurriness”) leading to a (near) disappearance of the original well-defined dispersions. Thus intriguingly, PdCrO_2 at hypothetical *smaller* U is a very incoherent metal (or “bad metal”), apparently evading Fermi-liquid characteristics and seemingly in conflict with Luttinger’s theorem. Coherence in the cPd band is reached at larger U when the CrO_2 layers are Mott insulating, which again under-

lines the intricate coupling between the Pd and the CrO_2 layers. Substitutional doping of the Cr site by isovalent Mo could be a way to reach a lower effective U value in the system.

B. Designed heterostructures

For the heterostructures $\text{Pd}_n\text{Ag}_m\text{CrO}_2$, supercells of $1 \times 1 \times 3$ kind (12 basis atoms) for $n \neq m$ and of $1 \times 1 \times 2$ kind (6 basis atoms) for $n = m = 1$ are constructed (see Fig. 1). The respective supercell lattice parameters are obtained from linear interpolation of the bulk parameters and the atomic positions are structurally optimized within DFT. The Hubbard U on the Cr site is also chosen to result from a linear interpolation of the respective bulk values, i.e. $J_H = 0.7$ eV and $U(\text{P2A}) = 3.33$ eV,

$$U(\text{PA}) = 3.50 \text{ eV}, U(\text{PA}2) = 3.67 \text{ eV}.$$

1. At room temperature: $T = 290 \text{ K}$

In order to first address the phase stability, the electronic formation energy

$$E_{\text{form}}^{(nm)} = E_{\text{tot}}(\text{Pd}_n\text{Ag}_m\text{CrO}_2) - nE_{\text{tot}}(\text{PdCrO}_2) - mE_{\text{tot}}(\text{AgCrO}_2), \quad (1)$$

where E_{tot} are the total energies either in DFT or DFT+DMFT, may be considered. Note that here, we aligned the plane-wave energy cutoff E_{cut} to obtain comparable total energies. Within DFT, all designed heterostructures yield a negative E_{form} , thus the considered phases are stable against decomposition into a mixture of the bulk phases. Within DFT+DMFT, only the P2A structure has a negative formation energy, but the absolute values of the order of $\sim 10 \text{ meV/atom}$ are rather small throughout the series. Note that the given $E_{\text{form}}^{(nm)}$ should only be interpreted as a rough guide for phase stability, since the latter depends furthermore on the temperature window, the entropy, the vibrational free energy and further nano-structuring effects, i.e. given through thin-film architectures. Therefore in summary, we consider the given $\text{Pd}_n\text{Ag}_m\text{CrO}_2$ phases as indeed serious candidates for stable heterostructures in experiment.

In bulk PdCrO_2 , the CrO_2 layers apparently do not severely harm the itinerancy of the free Pd electron, the established Mott-insulating layers even tend to stabilize the weakly-correlated cPd dispersion (see last paragraph of section II A). The present heterostructuring then formally poses a rather unique canonical problem: the single highly-itinerant electron, derived from the Pd layer, faces additional strong driving towards non-itinerant behavior imposed *outside* its hosting layer via the blocking layers of coupled Ag-CrO₂ kind. Standard mechanisms of

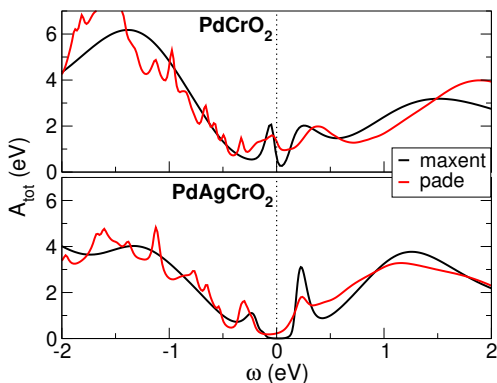


FIG. 6. (color online) Comparison between the total \mathbf{k} -integrated spectral functions obtained from analytical continuation via maximum-entropy and via Padé scheme for PdCrO_2 (top) and PdAgCrO_2 (bottom). The displayed Padé data results from a straightforward \mathbf{k} -sum of $A(\mathbf{k}, \omega)$ on a uniform \mathbf{k} -mesh in the respective Brillouin zone.

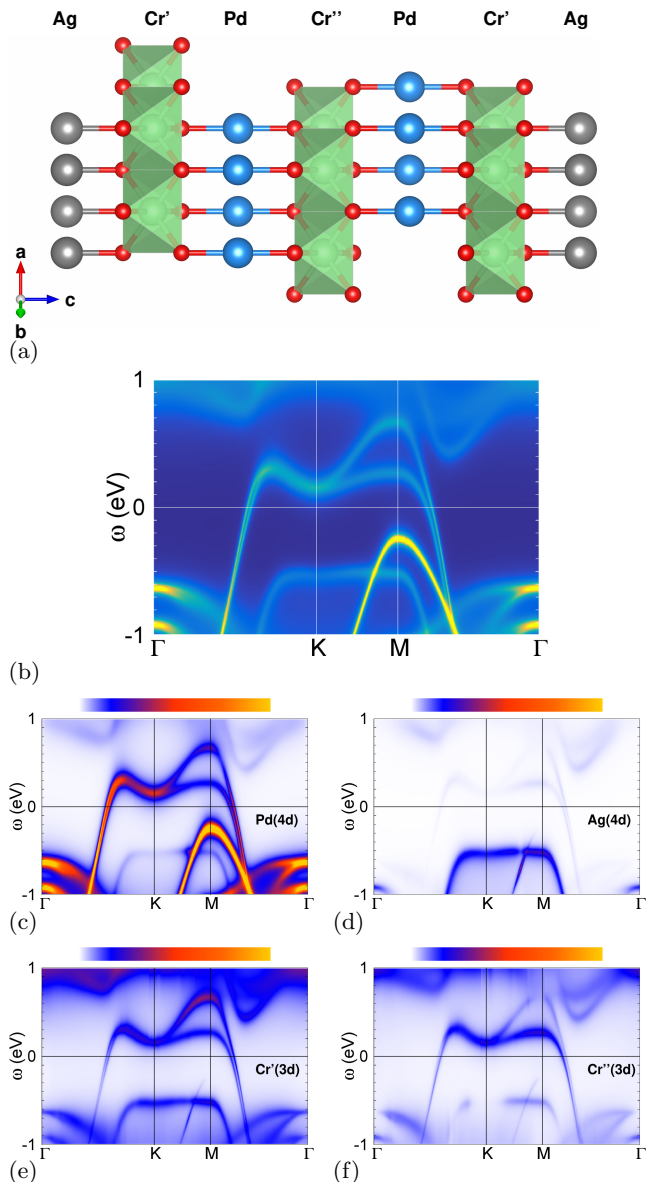


FIG. 7. (color online) Details on the $\text{Pd}_2\text{AgCrO}_2$ physics. (a) Crystal structure with vertical c -axis, displaying the symmetry-inequivalent Cr' and Cr'' layers (color coding as Fig 1). (b) Low-energy blow up of the \mathbf{k} -resolved spectral function along high-symmetry lines. (c-f) Site- and orbital-resolved spectral-function weight: (c) $\text{Pd}(4d)$ (d) $\text{Ag}(4d)$, (e) $\text{Cr}'(3d)$ and (f) $\text{Cr}''(3d)$.

creating “heaviness” for such an electron are not easily applicable, yet simply ignoring those new boundary conditions is neither an option. How does the electron cope with the new situation at room temperature?

The spectral information for the three heterostructures is summarized in Fig. 5. From the \mathbf{k} -resolved low-energy dispersions in Figs. 5a,d,g nothing spectacular seems to happen, there are still similar “low-energy bands” at ε_F , reminiscent of the PdCrO_2 bulk case. However surprisingly, the \mathbf{k} -integrated spectra (see also Figs. 5c,f,i) of

all three designed heterostructures show a pseudogap-like structure reaching zero spectral weight at ε_F . This gap feature is of size ~ 0.2 eV for P2A and PA, and about ~ 0.1 eV for PA2. It is important to point out that this at first seemingly contradicting findings of \mathbf{k} -resolved vs. \mathbf{k} -integrated spectra are not an artifact of the analytical continuation from Matsubara to real frequencies, but well-reproducible both with maximum-entropy as well as with Padé schemes. This is shown in Fig. 6, depicting a comparison of the maximum-entropy vs. Padé-derived spectrum for bulk PdCrO₂ and heterostructure PdAgCrO₂. While the straightforward \mathbf{k} -integrated Padé-based spectrum is more 'wiggly', the key result at low energy is identical: whereas in PdCrO₂ a quasiparticle feature crosses ε_F , PdAgCrO₂ shows a gap(-like) feature at $\omega = 0$.

In fact, there is no contradiction between the \mathbf{k} -resolved and the \mathbf{k} -integrated spectrum. The physical scenario is best coined by the term *correlation-induced semimetal (CIS)*, where electronic correlations suppress the low-energy spectral weight in a non-trivial dispersion setting. In a correlated system, a dispersion always carries spectral weight less than unity (contrary to e.g. a DFT picture), and in the present case the spectral weight associated with the dispersion crossing ε_F is exceptionally small at room temperature. Figures 5c,f,i show that most of the expected low-energy spectral weight piles up in sidebands at $\sim \pm 0.2$ eV. Note that this specific low-energy behavior is due to the unique coupling of originally weakly correlated Pd-based and strongly correlated Cr-based contributions in the (Pd,Ag)CrO₂ system. This coupling leads to low-energy dispersions of very weak spectral weight, resulting in negligible Fermi-level contribution upon \mathbf{k} integration.

Each Fermi-surface sheet, two in the case of P2A, still effectively encompasses one electron, respectively (cf. Figs. 5b,e,h). Only for the PA2 heterostructure the Γ -centered hole sheet, intriguingly, appears slightly enlarged, and we will come back to that observation in the next section.

A further aspect is noteworthy, and can be elaborated best from inspection of the P2A electronic structure with a subtle twofold dispersion crossing ε_F (cf. Fig. 7b). Figure 7a highlights the fact that there are two symmetry-inequivalent Cr layers: Cr'O₂ sandwiched by Ag and Pd layers as well as Cr''O₂ sandwiched by two Pd layers. The twofold dispersion crossing the Fermi level along Γ -K and M- Γ is nonsurprisingly of dominant Pd(4d) character as shown in Fig. 7c. The low-energy Ag(4d) weight accumulates in an occupied flat-band part along K-M with no relevant contribution right at ε_F (see Fig. 7d). While the Cr' weight is balanced between the twofold dispersion crossing ε_F , the Cr'' weight breaks this symmetry and attains somewhat larger weight on the FS sheet with slightly larger k_F (see Fig. 7e,f). Hence within the challenging correlation physics of the present delafossite heterostructures, there is furthermore an intricate hybridization component.

2. Below room temperature

The CIS state at room temperature is expectedly the result of a very low coherence scale of an underlying effectively doped Mott-insulating state of the CrO₂ layers. The DFT+DMFT calculations at lower temperature are numerically especially demanding for the multi-site five-orbital correlated subspaces in the heterostructure design. But indeed, below room temperature, a low-energy resonance emerges in the total spectral function of the delafossite heterostructures (see Fig. 8a). Notably, this resonance is now of dominating Cr character, and carries sizable Pd weight only for the P2A structure (see Fig. 8, right). Thus the given delafossite heterostructures are rather sensitive to temperature and display a semimetal-to-doped-Mott-insulator transition around 190 K.

A minimal picture behind these numerical results may be as follows. Heterostructuring of PdCrO₂ and AgCrO₂ leads to an effective doping of the CrO₂ layers, thus charge fluctuations between the Pd layers and the latter increase. Since the hopping *within* the Pd layers does not become heavily dressed in the Hubbard sense, the cPd dispersion is not strongly renormalized. In other

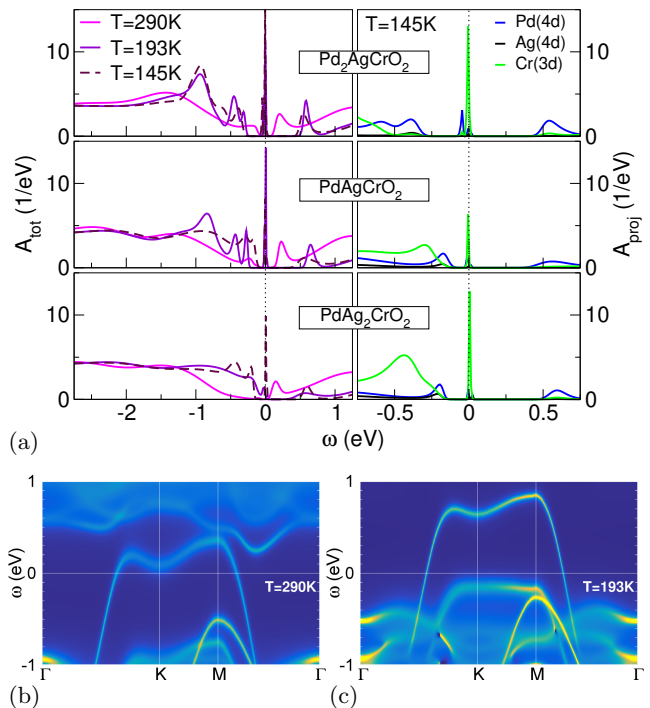


FIG. 8. (color online) Temperature-driven electronic transition in the delafossite heterostructures. (a) Evolution of the total spectral function with temperature throughout the series. Left: $A_{\text{tot}}(\omega)$ for P2A (top), PA (middle) and PA2 (bottom) at $T = 290$ K, 193 K and 145 K. Right: Element-specific projected spectral function at low energy for $T = 145$ K (same structure ordering as left part). (b,c) Low-energy \mathbf{k} -resolved function of PdAg₂CrO₂ for (b) $T = 290$ K and (c) $T = 193$ K.

words, there is no strong cPd band-narrowing effect, as seen in Fig. 5a,d,g. Instead, spectral-weight transfer away from low energy and loss of coherence occurs for an only weakly modified cPd dispersion. Still, the scattering with the doped CrO₂ layers is effective in marking a semimetallic scenario. At lower temperatures, the excitations in the doped-Mott layers eventually become coherent and a resonance appears at low energy.

Finally, let us remark on the fermiology of PA2. As obvious from Fig. 8, the PA2 structure develops a low-energy resonance at T lower than the other two heterostructures. At room temperature, the PA2 structure is furthest away from the doped-Mott coherence state. Low-energy coherence of the Mott layers, in the sense previously discussed for Fig. 4, is thus also not yet fully established at that higher T . Therefore, the PA2 Fermi surface in Fig. 5h shows the deviation from the expected sheet size. Only at lower temperature, when coherence is reinforced, the expected sheet size for one electron is established. This is visualized in the temperature comparison of the low-energy dispersions in Figs. 8b,c.

III. CONCLUSIONS AND DISCUSSION

Delafossite materials, and especially the metallic ones, are not only highly interesting in stoichiometric bulk form. In this paper we have shown that tailored heterostructuring of metallic PdCrO₂ and insulating AgCrO₂ gives rise to a plethora of challenging physics. The explicit aspect of electronic correlation, which is present but to a large extent hidden within the bulk compounds, takes over in the heterostructure phases Pd_{*n*}Ag_{*m*}CrO₂ and renders the demanding rivalry between metallicity and insulating tendencies strikingly obvious. Correlation-induced semimetallic states at room temperature and a transition to a doped Mott-insulating regime with low coherence scale at lower temperature have been revealed. Furthermore, layer-selective hybridization may play a decisive role in order to select the stable many-body states at low energy. Eventual com-

petition with antiferromagnetic spin-ordering tendencies upon further lowering T will even enlarge the scenario of competing many-body instabilities. But already without even considering possible magnetic ordering, there are many relevant degrees of freedom enabling a fascinating playground for very rich physics in designed delafossite heterostructures. An interesting route for investigations could be given by uniaxial-pressure experiments²⁸⁻³⁰. Either to modify the Hubbard U on Cr to reach the intricate non-Fermi-liquid regime at smaller U (cf. Fig. 4), or to effectively metallize the Mott layers by effective bandwidth enlargement. Moreover, the construction of explicit topological states within a Mott-critical background may be possible from further tailored heterostructure design.

Still, the question concerning experimental realization of these and further delafossite heterostructures arises. The representation of delafossites with standard growth techniques has been proven challenging. However the recent growth of PdCoO₂ by molecular beam epitaxy³¹ is encouraging and should pave the road for a future realization of delafossite heterostructures. In addition, single-layer deposition onto suitable terminated bulk delafossites may already prove helpful in creating exciting electron states on a surface (see e.g. Ref. 32 for work in that direction).

Let us conclude by the final remark that the key metal-delafossite physics of a crucial coupling between weakly itinerant layers and strongly correlated (Mott) layers connects also to the recent finding of superconductivity in infinite-layer nickelate upon hole doping³³, where similar scenarios might be at play at stoichiometry.

ACKNOWLEDGMENTS

We thank A. P. Mackenzie and V. Sunko for helpful discussions. Financial support from the DFG LE-2446/4-1 project “Design of strongly correlated materials” is acknowledged. Computations were performed at the JUWELS Cluster of the Jülich Supercomputing Centre (JSC) under project number hhh08.

¹ R. D. Shannon, D. B. Rogers, and C. T. Prewitt, *Inorg. Chem.* **10**, 713 (1971).

C. T. Prewitt, R. D. Shannon, and D. B. Rogers, *Inorg. Chem.* **10**, 719 (1971).

D. B. Rogers, R. D. Shannon, and C. T. Prewitt, *Inorg. Chem.* **10**, 723 (1971).

² H. Kawazoe, M. Yasukawa, H. Hyodo, M. Kurita, H. Yanagi, and H. Hosono, *Nature* **389**, 939 (1997).

³ S. Seki, Y. Onose, and Y. Tokura, *Phys. Rev. Lett.* **101**, 067204 (2008).

⁴ N. Terada, D. D. Khalyavin, P. Manuel, Y. Tsujimoto, K. Knight, P. G. Radaelli, H. S. Suzuki, and H. Kitazawa, *Phys. Rev. Lett.* **109**, 097203 (2012).

⁵ S. Ouyang, Z. Li, Z. Ouyang, T. Yu, J. Ye, and Z. Zou, *J. Phys. Chem. C* **112**, 3134 (2008).

⁶ A. P. Mackenzie, *Rep. Prog. Phys.* **80**, 032501 (2017).

⁷ R. Daou, R. Frésard, V. Eyert, S. Hébert, and A. Maignan, *Science and Technology of Advanced Materials* **18**, 919 (2017).

⁸ H. Takatsu, H. Yoshizawa, S. Yonezawa, and Y. Maeno, *Phys. Rev. B* **79**, 104424 (2009).

⁹ H.-J. Noh, J. Jeong, B. Chang, D. Jeong, H. S. Moon, E.-J. Cho, J. M. Ok, J. S. Kim, K. Kim, B. I. Min, et al., *Sci. Rep.* **4**, 3680 (2014).

¹⁰ F. Lechermann, *Phys. Rev. Materials* **2**, 085004 (2018).

¹¹ V. Sunko, F. Mazzola, S. Kitamura, S. Khim, P. Kushwaha, O. J. Clark, M. Watson, I. Markovic, D. Biswas, L. Pourovskii, et al., *Sci. Adv.* **6**, eaaz0611 (2020).

¹² H. Takatsu, S. Yonezawa, C. Michioka, K. Yoshimura, and Y. Maeno, *J. Phys. Conf. Ser.* **200**, 012198 (2010).

- ¹³ S. Y. Savrasov, G. Kotliar, and E. Abrahams, *Nature* **410**, 793 (2001).
- ¹⁴ L. V. Pourovskii, B. Amadon, S. Biermann, and A. Georges, *Phys. Rev. B* **76**, 235101 (2007).
- ¹⁵ D. Grieger, C. Piefke, O. E. Peil, and F. Lechermann, *Phys. Rev. B* **86**, 155121 (2012).
- ¹⁶ S. G. Louie, K. M. Ho, and M. L. Cohen, *Phys. Rev. B* **19**, 1774 (1979).
- ¹⁷ B. Meyer, C. Elsässer, F. Lechermann, and M. Fähnle, *FORTRAN 90 Program for Mixed-Basis-Pseudopotential Calculations for Crystals*, Max-Planck-Institut für Metallforschung, Stuttgart (1998).
- ¹⁸ J. P. Perdew, K. Burke, and M. Ernzerhof, *Phys. Rev. Lett.* **77**, 3865 (1996).
- ¹⁹ B. Amadon, F. Lechermann, A. Georges, F. Jollet, T. O. Wehling, and A. I. Lichtenstein, *Phys. Rev. B* **77**, 205112 (2008).
- ²⁰ V. I. Anisimov, D. E. Kondakov, A. V. Kozhevnikov, I. A. Nekrasov, Z. V. Pchelkina, J. W. Allen, S.-K. Mo, H.-D. Kim, P. Metcalf, S. Suga, et al., *Phys. Rev. B* **71**, 125119 (2005).
- ²¹ A. N. Rubtsov, V. V. Savkin, and A. I. Lichtenstein, *Phys. Rev. B* **72**, 035122 (2005).
- ²² P. Werner, A. Comanac, L. de' Medici, M. Troyer, and A. J. Millis, *Phys. Rev. Lett.* **97**, 076405 (2006).
- ²³ O. Parcollet, M. Ferrero, T. Ayrál, H. Hafermann, I. Krivenko, L. Messio, and P. Seth, *Comput. Phys. Commun.* **196**, 398 (2015).
- ²⁴ P. Seth, I. Krivenko, M. Ferrero, and O. Parcollet, *Comput. Phys. Commun.* **200**, 274 (2016).
- ²⁵ V. I. Anisimov, I. V. Solovyev, M. A. Korotin, M. T. Czyżyk, and G. A. Sawatzky, *Phys. Rev. B* **48**, 16929 (1993).
- ²⁶ J. A. Sobota, K. Kim, H. Takatsu, M. Hashimoto, S.-K. Mo, Z. Hussain, T. Oguchi, T. Shishidou, Y. Maeno, B. I. Min, et al., *Phys. Rev. B* **88**, 125109 (2013).
- ²⁷ E. Pavarini, S. Biermann, A. Poteryaev, A. I. Lichtenstein, A. Georges, and O. K. Andersen, *Phys. Rev. Lett.* **92**, 176403 (2004).
- ²⁸ S. Riccò, M. Kim, A. Tamai, S. M. Walker, F. Y. Bruno, I. Cucchi, E. Cappelli, C. Besnard, T. K. Kim, P. Dudin, et al., *Nat. Commun.* **9**, 4535 (2018).
- ²⁹ V. Sunko, E. A. Morales, I. Marković, M. E. Barber, D. Milosavljević, F. Mazzola, D. A. Sokolov, N. Kikugawa, C. Cacho, P. Dudin, et al., arXiv:1903.09581 (2019).
- ³⁰ M. E. Barber, F. Lechermann, S. V. Streltsov, S. L. Skornyakov, S. Ghosh, B. J. Ramshaw, N. Kikugawa, D. A. Sokolov, A. P. Mackenzie, C. W. Hicks, et al., arXiv:1909.02743 (2019).
- ³¹ M. Brahlek, G. Rimal, J. M. Ok, D. Mukherjee, A. R. Mazza, Q. Lu, H. N. Lee, T. Z. Ward, R. R. Unocic, G. Eres, et al., *Phys. Rev. Materials* **3**, 093401 (2019).
- ³² F. Mazzola, V. Sunko, S. Khim, H. Rosner, P. Kushwaha, O. J. Clark, L. Bawden, I. Marković, T. K. Kim, M. Hoesch, et al., *PNAS* **115**, 12956 (2018).
- ³³ D. Li, K. Lee, B. Y. Wang, M. Osada, S. Crossley, H. R. Lee, Y. Cui, Y. Hikita, and H. Y. Wang, *Nature* **572**, 624 (2019).